AIAA JOURNAL
Vol. 38, No. 2, February 2000

Correlation of Helicopter Rotor Tip Vortex Measurements

Mahendra J. Bhagwat* and J. Gordon Leishman†
University of Maryland, College Park, Maryland 20742

The roll-up and development of the tip vortices generated by subscale helicopter rotors were measured and analyzed. The measurements were performed on one- and two-bladed hovering rotors using three-component laser Doppler velocimetry. A trip strip was used to simulate boundary-layer transition at the higher Reynolds numbers typical of the full-scale rotor. The detailed velocity field of the tip vortex was investigated, a strong self-similarity of the swirl velocity profile being found. The measurements suggest a general logarithmic growth of the viscous core, which for older vortex ages is proportional to the square root of time (vortex age). Measurements from other helicopter rotor and fixed-wing experiments are used to support the observations.

Nomenclature

A	= rotor disk area, πR^2, m^2
C_T	= thrust coefficient, $T/\rho A\Omega^2 R^2$
c	= rotor blade chord, m
$\bar{d}$	= nondimensional distance, $\zeta\Gamma_v/(\Omega c^2)$
N_b	= number of blades
R	= rotor radius, m
r	= radial distance, m
$\bar{r}$	= nondimensional radial distance, r/r_c
r_c	= vortex core radius, m
T	= rotor thrust, N
t	= time, s
V_θ	= swirl (tangential) velocity, m s^{-1}
$V_{\theta_{\max}}$	= peak swirl velocity, m s^{-1}
$\bar{V}_{\theta_{\max}}$	= nondimensional peak velocity, $V_{\theta_{\max}} c/\Gamma_v$
x, y, z	= rotor coordinate system, m
x_T, y_T, z_T	= traverse coordinate system, m
Γ	= circulation, m^2 s^{-1}
Γ_c	= vortex core circulation, $2\pi V_{\theta_{\max}} r_c$, m^2 s^{-1}
Γ_v	= net vortex circulation, m^2 s^{-1}
δ	= turbulent viscosity coefficient
ζ	= vortex age, deg
$\bar{\zeta}$	= equivalent vortex age, $N_b\zeta$, deg
ν	= kinematic viscosity, m^2 s^{-1}
ρ	= flow density, kg m^{-3}
σ	= rotor solidity, $N_b c/\pi R$
Ω	= rotor rotational frequency, rad s^{-1}

Introduction

THE blade-tip vortices are aerodynamically the most significant, but perhaps the most intricate and poorly understood, features of a helicopter rotor wake, e.g., Ref. 1. The strengths, induced velocity field, and spatial locations and orientations of the vortices relative to the rotor affect blade loads, rotor performance (i.e., thrust and power), and rotor noise levels. Under many flight conditions, especially during maneuvers and descending flight, the blades interact closely with tip vortices generated by other blades, resulting in a phenomenon known as blade vortex interaction (BVI). BVI produces three-dimensional unsteady airloads that can manifest as high rotor vibrations and strong impulsive noise.[2] The tip vortices can also affect the induced airloads on the helicopter fuselage[3] or the tail rotor and empennage assembly.[4] These complex vortex/airframe interactions can lead to aerodynamic-induced airframe vibrations, losses in rotor performance, and an overall degradation in the handling qualities of the helicopter. Therefore, one key to improved predictions of many helicopter-related problems lies in a better understanding and modeling capability of the blade-tip vortices.

Several numerical models have been developed to represent the vortical rotor wake and its effects on the aerodynamic environment around the helicopter. These models range from integral momentum approaches to modern computational fluid dynamics based on finite difference techniques. The free-vortex methodology or free-wake[5–11] has emerged as one of the most practical methods because it can provide a high-fidelity wake solution at modest computational expense, as well as minimizing dependence on empirical factors. In a typical free-wake method the discretized wake filaments evolve in a force-free manner according to Helmholtz's law under the action of an induced velocity field resulting from all of the vortex filaments in the surrounding flow. In effect, the process of vortex convection is separated from other viscous mechanisms. This, however, presumes an a priori knowledge of the vortex roll up as well as any subsequent viscosity related growth characteristics, e.g., the circulation strength and the viscous core size of the tip vortex as a function of wake age. Therefore, the success of free-wake methods as an analysis or design tool depends not only the ability to convect the tip vortices accurately, but also on the ability to model vortex and its viscous growth characteristics. Key modeling issues are the vorticity and velocity field surrounding the vortex core and the diffusive/dissipative time scales. In most cases these parameters have been modeled semi-empirically based on information extracted, extrapolated, or otherwise assumed from measurements performed on fixed (nonrotating) wing-generated vortices, e.g., Refs. 12 and 13. Corresponding measurements of the tip vortex flows generated by rotors have not yet been obtained in sufficient quality and quantity. This is, in part, because of the highly time-varying and three-dimensional nature of the rotor flowfield (e.g., Ref. 1), which stretches the limitations of most flow diagnostic instrumentation.

Laser Doppler velocimetry (LDV) offers an accurate and versatile measurement technique, and its nonintrusive nature makes it most suitable for rotating-wing experiments.[14–21] One-, two-, and three-component systems have been used for rotor flowfield measurements. However, one- and two-component LDV systems tend to suffer from reduced spatial resolution because of elongated measurement volumes, more so with large stand-off distances. Three-component LDV systems can, at least potentially, deliver extremely high spatial accuracy. Seelhorst et al.[18] have conducted three-component LDV tests in the wake of subscale helicopter rotor with emphasis on the effects of blade tip shape. McAlister and colleagues[21,22] have used a three-component LDV to measure the velocities in the near wake of a hovering rotor, although only at three vortex ages. Han et al.,[16] Coyne et al.,[17] and Leishman et al.[23] have measured the velocity field and turbulence structure of the tip vortex generated by a one-bladed rotor using three-component LDV. The results have documented the swirl (tangential) and axial velocity profiles of the tip vortex at several vortex ages.

Received 30 April 1998; revision received 15 May 1999; accepted for publication 8 July 1999.

*Graduate Research Assistant, Department of Aerospace Engineering, Glenn L. Martin Institute of Technology.

†Associate Professor, Department of Aerospace Engineering, Glenn L. Martin Institute of Technology.

The objective of the present work is to provide further physical insight into the structure of helicopter rotor-tip vortices, with a goal of providing a basis for improved modeling in many forms of rotor analysis. Measurements are performed using three-component LDV. The results for three rotor configurations are compared and contrasted. Correlations obtained suggest a relatively general vortex structure and diffusive growth trend. The results are also compared with experimental results from other sources,[20,21] which are shown to be in good general agreement with the diffusive core growth trend suggested by the present measurements.

Description of the Experiment

Rotor System

The experimental setup consisted of a teetering type subscale helicopter rotor operating in hover. The one-bladed rotors used a counter balance weight for dynamic balance, whereas the two-bladed rotor used a set of matched blades. Untwisted blades with a rectangular planform were used to keep the thrust distribution biased toward the blade tip to produce a relatively strong tip vortex. The operating conditions for the rotors were chosen to match the blade loading C_T/σ, so as to generate tip vortices with the same nominal strengths (circulation), Γ_v. In each case the rotor-tip Mach number was approximately 0.26, with a corresponding tip chord Reynolds number of 2.7×10^5. The operating conditions for the different rotor configurations are summarized in Table 1. A boundary-layer trip was used on the one-bladed rotor to simulate the transition point found at full-scale rotor Reynolds numbers.

LDV System

A fiber-optic-based LDV system was used to make measurements of the velocity field. Three pairs of laser beams (green, blue, and violet) were used to measure simultaneously all three components of velocity. The three pairs of beams were carefully focused at a point in space with the aid of a microscope objective lens. The measurement volume thus formed is defined by the intersection of the three ellipsoidal beam crossing volumes (Fig. 1). The major axis of this ellipsoidal volume is related to the beam crossing angles, with the minor axis being related to the beam diameters (in this case, approximately 73 μm based on the Gaussian $1/e^2$ energy distribution).

Table 1 Operating conditions for the rotor configurations

Parameter	Rotor		
	One bladed	Two bladed	One bladed[a]
Number of blades	1	2	1
Rotor speed	2100 rpm	2010 rpm	2060 rpm
	35 Hz	33.5 Hz	34.3 Hz
Blade radius	406.4 mm	406.4 mm	406.4 mm
Blade chord	42.5 mm	42.5 mm	44.3 mm
Collective pitch	4 deg	5 deg	4 deg
C_T (estimated)	0.003	0.006	0.003

[a]Boundary-layer transition point fixed.

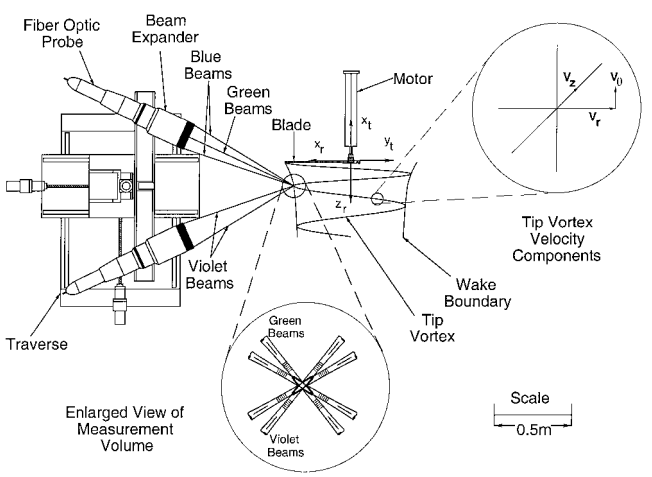

Fig. 1 Schematic of LDV system and rotor showing global traverse and local tip-vortex coordinate systems.

Two modes of LDV data acquisition are possible: random mode and coincidence mode. In the former mode the three velocity components are uncorrelated and independent of each other. This mode generally provides a lower spatial resolution, also with a preponderance of data on one component. In coincidence mode, which is the acquisition mode used here, the velocity measurements are obtained simultaneously and are statistically correlated. Data acquisition is also limited to a time window where digital processors on all three channels need to recognize a data point simultaneously. This ensures that the velocities measured are from the same particle. Furthermore, in coincidence mode the effective LDV measurement volume is of the order of the beam diameter, as defined by the three pairs of intersecting ellipsoids from each of the green, blue, and violet beam pairs. Therefore, this acquisition mode gives superior spatial resolution as compared to either one- or two-component systems (where the effective three-dimensional measurement volume is of the order of the major axis of the ellipsoidal volume) and is essential to measure accurately the high velocity gradients found inside the vortex cores.

The flowfield was seeded with atomized olive oil. From a calibration the atomizer was found to produce seed particles with a diameter of 0.8 μm with a standard deviation of 0.2 μm. This consistent, submicron size minimized any errors in velocity field measurements resulting from acceleration effects on the seed particles (see Ref. 24 for a detailed analysis of this problem). For the present flow, these errors are negligible. The scattered light from seed particles crossing the interference fringes was collected by the receiving optics and coupled to a set of photomultipliers through fiber-optic receiving fibers. A real-time autocorrelator computed the Doppler frequency for each channel, which were subsequently transformed into three orthogonal velocity components. A rotating machinery resolver interface used the one-per-revolution (1/rev.) signal from the rotor to assess continuously the rotor phasing. This was used to calculate the blade azimuth position, which was digitally tagged to the velocity data. The azimuth-tagged data were then sorted into 400 discrete bins (i.e., an azimuthal resolution of 0.9 deg per bin). A phase-locked loop processor ensured that the data were free from any errors introduced by slight variations in the rotational speed of the rotor. Further details of the general setup can be found in Refs. 16 and 23.

A source of uncertainty in making velocity measurements in the tip vortex core is the aperiodic nature of the rotor wake, similar to the wandering or meandering in the fixed-wing case.[25] The aperiodic motion of the tip vortices causes an averaging effect, therefore resulting in a smaller swirl velocity in the tip vortex and also a larger effective core size. It is possible to estimate this uncertainty and, in in some cases, to correct the measured velocity field for these effects using deconvolution techniques.[25,26] For the present measurements the maximum uncertainty resulting from aperiodicity at vortex ages of less then one rotor revolution were determined to be at most 5%, i.e., the measured core size was at most overestimated by 5% and the measured velocity peaks at most underestimated by 5%. For vortex ages between one and two revolutions, the maximum uncertainty increased to 10% and to about 20% for vortex ages older than two revolutions.

Boundary-Layer Trip

The difficulties in conducting correlated three-component phase-resolved LDV measurements presently restrict the technique to subscale helicopter rotor models. This, however, raises several questions about Reynolds-number scaling. The blade Reynolds number governs the boundary-layer thickness, the points of transition and separation, and also the thickness of the shear layer in the wake behind the blade. The inability to match the laminar to turbulent transition point is probably a more serious cause of scale effects.[27] There is a further complication because of the need to address the scaling effects of vortex Reynolds number Γ_v/ν. This aspect of the problem, however, is not addressed in the present work.

One method of predetermining the boundary-layer transition point is by using a trip strip or distributed surface roughness.[28,29] Because the Reynolds number varies along the span of the blade, there is no established practice for using boundary-layer trips on rotors. However, standard practice for fixed-wing experiments dictates that

the height of the trip or roughness should be calculated based on the critical Reynolds number required for transition to turbulence.[30,31] The results reported in Refs. 28, 29, and 32 were used as guidelines to design trip strips for the rotor tests. A trip strip was preferred over distributed surface roughness to avoid the possibilities of premature separation of the turbulent boundary-layer downstream of the transition point.

The height of the trip strip was chosen to be of the order of the estimated laminar boundary-layer thickness at each station along the blade. Because the Reynolds number varies along the blade span, both the trip height and width must be varied. The trip strip was located at 2% chord from the leading edge of the blade on the upper surface and at 20% chord on the lower surface. The height of the trip was of the order of the predicted laminar boundary-layer thickness at that chordwise station. The trip was fabricated using 320-grit aluminum oxide particles near the blade tip, which progressively transitioned to 240-grit carborundum particles further inboard. The width of the strip was increased linearly from 2% chord at the blade tip to 4% chord near the root.

Test Procedure

Light sheet/smoke flow visualization was used to target the locations of the tip vortices. These results were used to center the LDV measurement grid about the vortex axis at each measurement plane. A traverse grid was generated with a 1-mm (2.4% of chord) spacing away from the viscous core region and less than a 0.2-mm (<0.5% of chord) spacing around the vortex core. In the first set of experiments, phase-resolved measurements were made over a complete rotor revolution, with up to 40 K coincident data samples per channel per grid point being specified. The nominally helical tip vortices generated by each blade convect along the wake boundary and pass through these grids, the axis (stagnation point) of the tip vortex becoming centered on the grid only at one particular vortex age. A second set of experiments was conducted to allow more detailed measurements of the tip vortex structure. In this case the measurements were also windowed in an azimuthal sense to a width of 45 deg (corresponding to 50 bins) centered around the same vortex age. This resulted in a much larger number of valid data samples in each bin and, therefore, improved the statistical accuracy of the measured velocity field. This windowing process is schematically illustrated in Fig. 2.

For the one- and two-bladed rotors tip vortex measurements were made at 14 vortex ages. This included measurements at vortex ages as young as 10 deg, which is within one chord of the blade trailing edge. Three-component measurements could not be made at earlier vortex ages because the trailing edge of the blade blocked optical access of one or more of the six laser beams. The oldest vortex age measured was at about two rotor revolutions. Beyond this point, the onset of interactions between elements of the vortices resulted in an increased aperiodic behavior of the rotor wake as it progressively degenerated into a turbulent jet. Coherent measurements, therefore, become increasingly difficult for very old vortex ages. Measurements at five vortex ages were made for the rotor with the transition point fixed by means of the boundary-layer trip. This allowed comparisons of overall trends as well as with the vortex characteristics at the corresponding vortex ages measured with the baseline rotor.

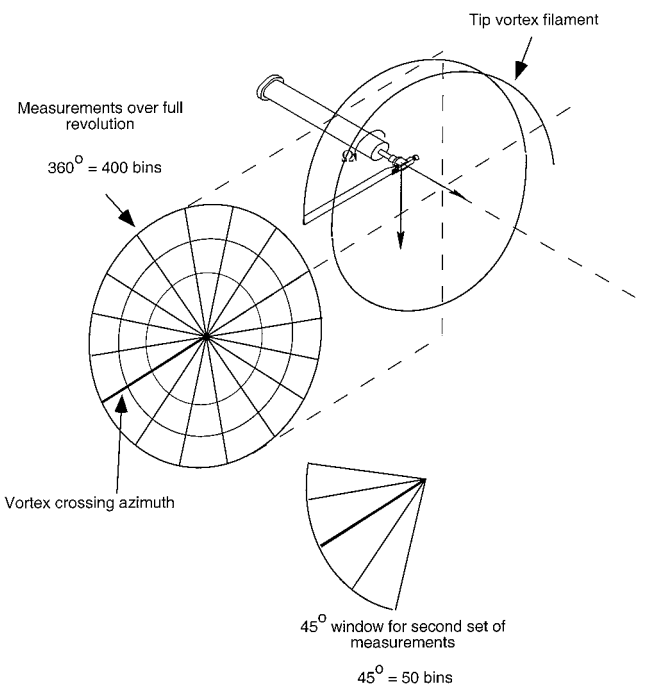

Fig. 2 Grids used for the two sets of phase-resolved measurements.

Results and Discussion

The tip vortex convects in a nonuniform flow that is induced by the rotor and its entire wake system. To analyze the properties of the trailed tip vortex itself, it is necessary to isolate it from the effects of the mean (time-averaged) flow. In a classical Reynolds-type decomposition the measured phase-resolved instantaneous velocity field can be considered to comprise of two components: a time-averaged convection velocity of the tip vortex through the flow and a residual induced velocity resulting from, in effect, the isolated tip vortex. In the present case the latter quantity has been computed by subtracting the time-averaged velocity measured over one rotor revolution from the instantaneous measurements at the same grid points. Figure 3 shows an example for the one-bladed rotor at a vortex age $\zeta = 102.2$ deg. The tip vortex lies on the boundary of a contracting jet-like wake. Therefore, the time-averaged measurements show a significant slipstream velocity inside the wake boundary, in this case with a maximum nondimensional value of about 0.06. Outside the wake boundary there is only a small velocity resulting from flow entrainment. When this time-averaged result is subtracted point-by-point from the instantaneous phase-resolved velocity field, the convection velocity is removed, and the resulting velocity field is essentially in a frame of reference that moves with the vortex. In this form the results are amenable to further analysis.

Velocity Field

Figures 4 and 5 show the residual swirl (tangential) velocities measured at several different vortex ages for the one- and two-bladed rotors, respectively. The asymmetry of the vortex flowfield is noteworthy, with a lower upwash on the outside and the higher downwash on the inside of the wake boundary. This implies that the rotor-tip vortex consists of noncircular streamlines with respect its axis (stagnation point), in contrast to the circular streamlines found in a rectilinear axisymmetric vortex. This is not an unusual result in vortex measurements and in this case can, in part, be attributed to the self-induced effects associated with the curvature and helical form of the tip vortex. This asymmetry has also been observed in other rotor measurements[20] and also some fixed-wing tip vortices,[33] the latter of which can be attributed to the presence of another vortex or a solid boundary.

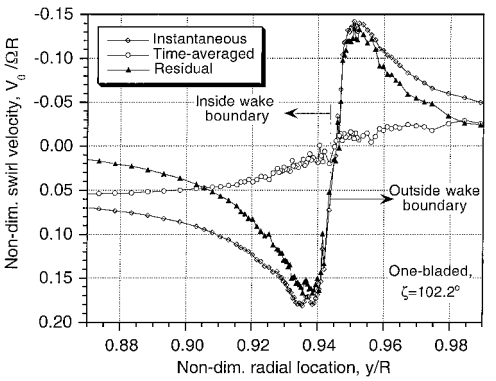

Fig. 3 Typical measurements of swirl velocity in the vortex when centered on the measurement grid: instantaneous, time averaged, and residual, $N_b = 1$, $\zeta = 102.2$ deg.

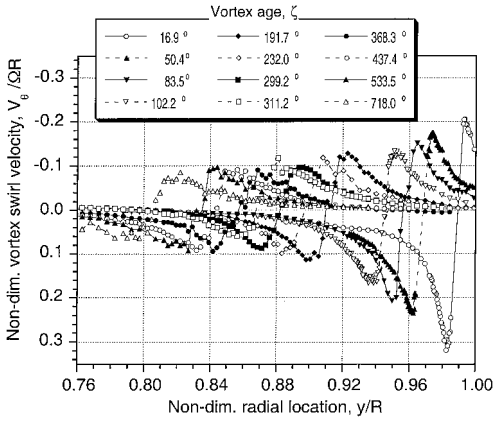

Fig. 4 Swirl velocity profiles induced by the tip vortex generated by the one-bladed rotor at various vortex ages.

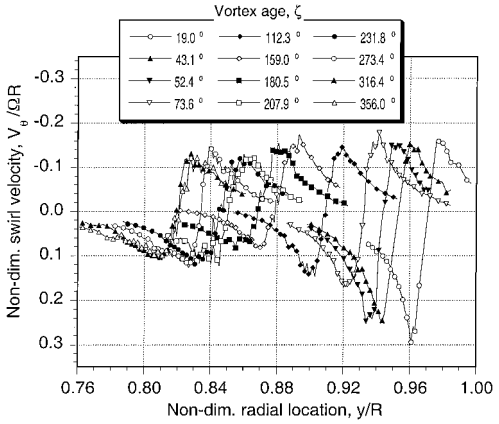

Fig. 5 Swirl velocity profiles induced by the tip vortex generated by the two-bladed rotor at various vortex ages.

Another significant observation from Figs. 4 and 5 is that the velocity peaks on either side of the vortex core asymptotically decrease as the vortex ages. This is indicative of vorticity diffusion, which results from the action of viscosity and turbulence generation within the vortex core. Proper quantification and documentation of the diffusion of tip vortices is a long-standing issue. There is a further complication in documenting such effects with helicopter rotor because of the influence of other blades and tip vortices. For example, the effects of close blade/vortex encounters, such as at the first blade passage at $\zeta = 360$ deg/ N_b, can introduce velocity gradients that can result in vortex stretching and vorticity intensification. This effect is suggested in Fig. 4 at $\zeta \approx 368$ deg and in Fig. 5 for $\zeta \approx 208$ deg, where there is a momentary increase in peak swirl velocity. For rotors with more than two blades, these effects are likely to be much more complicated and may even mask the underlying viscous diffusion trends.

Figure 6 shows the results of the peak swirl velocities in the tip vortex as a function of vortex age for the one-bladed rotor. The asymmetry of the velocity profile is biased toward the inner side of the wake boundary prior to the first blade passage ($\zeta = 360$ deg/ N_b). After the first blade passage, however, the velocity distributions become more symmetric. This initial asymmetry must result, in part, from self-induced velocity because of the curvature of the filaments with respect to the measurement grid. The basic effect of curvature will be a higher swirl velocity peak on the inner side (inside the slipstream boundary) than the outer side (cf., a vortex ring). Perhaps a less obvious reason for the asymmetry of the velocity profile is the high velocity gradients induced by the rotating blade. The average peak swirl velocity in Fig. 6 shows a decreasing trend as the vortex ages.

Figure 7 shows the average maximum swirl velocities measured in the tip vortices for the three rotor configurations that were tested. Note that the ordinate in this case is vortex age ζ times the number

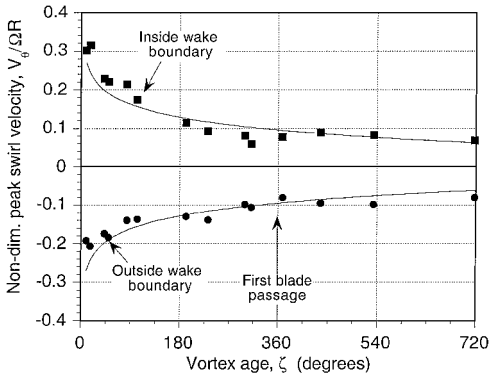

Fig. 6 Peak swirl velocity in the tip vortex as a function of vortex age for the one-bladed rotor.

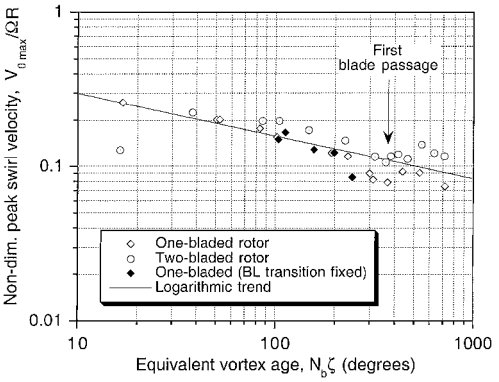

Fig. 7 Correlation of average peak swirl velocity as a function of equivalent vortex age.

of blades N_b. This equivalent vortex age ζN_b allows a comparison of the results on a timescale that gives coincident blade passage events. The results in Fig. 7 suggest that the core velocity decreases logarithmically as the vortex ages, which is a general characteristic of viscous diffusion. Similar trends have been observed in fixed-wing tip vortices, e.g., Ref. 34. Note, however, that at the first blade passage there is a noticeable change in the growth trend. As already explained, this is most likely an effect caused by the higher local velocity gradients produced as the blade and vortex come into proximity.

Core Growth

The vortex core dimension is an important parameter that is frequently used to define the structure and evolution of vortices. The core size is inversely related to the maximum induced swirl velocities and, therefore, can be used as an indicator as to the intensity of induced effects. Because, in general, the tip vortices remain in close proximity to helicopter rotors, more so in descents and maneuvers, an understanding of not only the initial core size after roll up but also the subsequent growth characteristics are very important.

Half the distance between the two velocity peaks on either side of the vortex can be considered as the nominal core radius. The approach used in the present analysis is to fix the vortex center at the stagnation point, where the vortex-induced swirl velocity is zero. Therefore, this results in a description of the vortex in terms of two unequal core radii on the inner and the outer sides of the vortex axis. From the velocity profiles shown in Figs. 4 and 5, the average core radius generally increases with increasing vortex age.

Figure 8 shows the average core radius as a function of equivalent vortex age for the one- and two-bladed rotors. A logarithmic scale is used on the ordinate to bring out the logarithmic nature of the growth trend, which as already mentioned, is a characteristic of viscous diffusion. The blade passage event temporarily reduces or reverses the growth trend, and a slight decrease in core size is observed after the first blade passage. This decrease in core size is more evident in case of the two-bladed rotor because the tip vortex is nearly twice as close to the following blade. After the blade passage the core

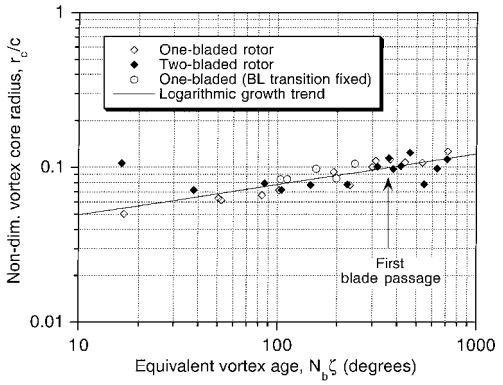

Fig. 8 Growth of the vortex core as a function of equivalent vortex age.

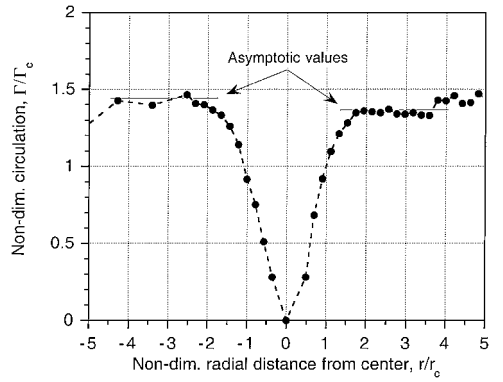

Fig. 9 Typical results showing the asymptotic values of circulation on the inner (wake) and outer (quiescent flow) side of the vortex axis: one-bladed rotor, $\zeta = 102.2$ deg.

continues to grow, although the growth is slower and more asymptotic. The core radii for the rotor with the boundary-layer transition point fixed were found to be slightly larger than for the baseline rotor. The peak swirl velocities, however, were approximately the same (see Fig. 7).

Vortex Circulation

Conventionally, the tip vortex is assumed to be axisymmetric, i.e., the circulation density $(V_\theta r)$ is assumed to be constant for each value of r, and the circulation is calculated from the closed loop integral as

$$\Gamma(r) = -\oint_0^{2\pi} V_\theta r \, \mathrm{d}\theta \approx -2\pi V_\theta r \qquad (1)$$

In the present case the tip vortex is nonaxisymmetric; therefore, an average circulation is calculated separately from measurements on opposing sides of the vortex axis. Typical results are shown in Fig. 9 for the one-bladed rotor at a vortex age of 102.2 deg. The tip-vortex circulation strength Γ_v was approximated as the average of the asymptotic values at large r on opposing sides. The advantage of fixing the vortex center at the stagnation point is that the circulation density near the vortex axis becomes symmetric, i.e., $(V_\theta r)^- = (V_\theta r)^+$.

Figure 10 show the average tip-vortex circulation as a function of the equivalent vortex age for the one- and the two-bladed rotors. The tip-vortex circulation is highest at early vortex ages and decreases only slowly with vortex age or remains nominally constant, thereby confirming that energy dissipation in the tip vortices is very small, at least over the first few rotor revolutions. Also there is a slight increase in circulation just after the first blade passage. For the rotor with the boundary-layer transition point fixed, the tip-vortex circulation was found to be slightly higher at earlier vortex ages; however, the overall trend was found to be the same as for the other two rotors.

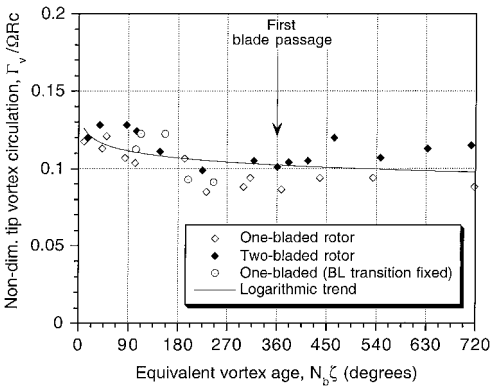

Fig. 10 Average tip-vortex circulation as a function of equivalent vortex age.

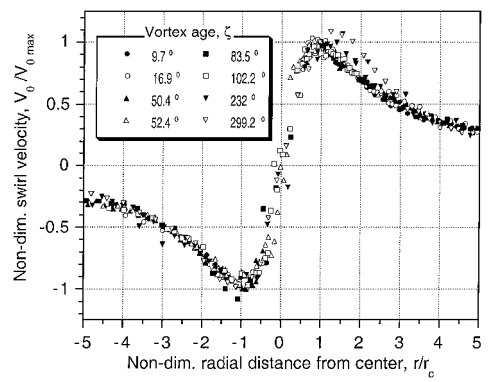

Fig. 11 Normalized vortex swirl velocity profiles for one-bladed rotor.

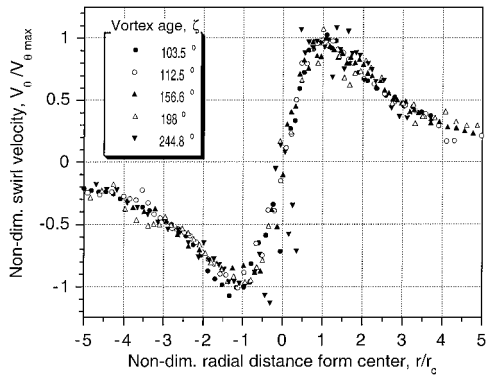

Fig. 12 Normalized vortex swirl velocity profiles for one-bladed rotor with boundary-layer transition fixed.

Self-Similarity of the Tip Vortex

Figures 11 and 12 show the swirl velocity normalized by the core swirl velocity, i.e., the peak swirl velocity and the radial distance normalized by the core radius. The reference velocity and length scales are different for different wake ages and also for the inner (slipstream) and outer sides of the tip vortex owing to the asymmetry. However, after normalizing in this manner, the velocity profiles collapse into one curve suggesting a strongly self-similar structure. This is an important confirmation of one aspect of modeling the tip vortex behavior, where the assumption of a self-similar velocity profile is frequently made, usually without validation.

Figures 13 and 14 show the normalized circulation profiles for the one- and two-bladed rotors, respectively. Here the circulation is normalized with the core circulation $2\pi V_{\theta_{\max}} r_c$. Again, the vortex exhibits a self-similar behavior, with the circulation distributions on either side of the vortex core at different vortex ages coalescing to a single curve. The results for the rotor with the transition point fixed indicate that the self-similar structure of the vortex is unaffected.

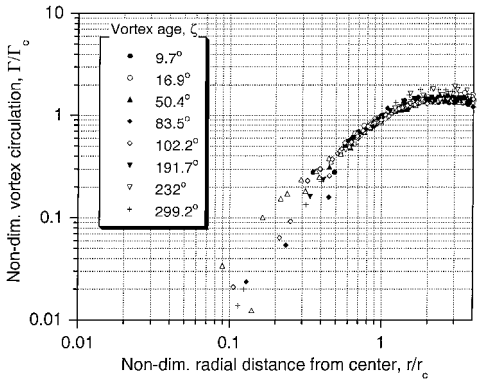

Fig. 13 Normalized tip-vortex circulation profiles for one-bladed rotor.

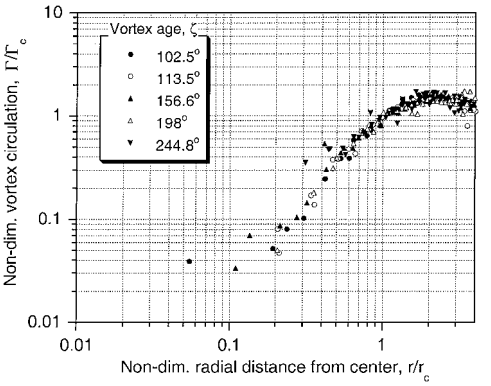

Fig. 14 Normalized tip-vortex circulation profiles for one-bladed rotor with boundary-layer transition fixed.

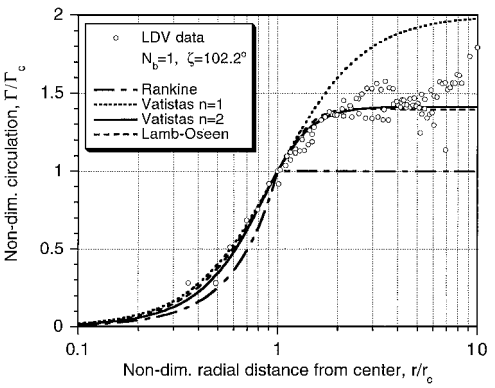

Fig. 15 Normalized circulation profiles using different analytic core models.

The circulation distribution in the vortex is analogous to the development of a boundary layer.[35] The inner core region, where the circulation varies as $\Gamma \propto r^2$, is similar to a laminar sublayer; a log region, where the circulation varies logarithmically, is similar to the law of the wall and an outer defect layer similar to the outer region in a fully developed turbulent boundary layer. The viscous core contains only about 70% of the total circulation in the tip vortex. This ratio is an important discriminator for the development of a model of the flow. The Rankine vortex, which assumes that all of the vorticity is concentrated within the viscous core, has a value of $\Gamma_v/\Gamma_c = 1.0$ (see Appendix). In the case of the Scully[36] and Vatistas[37] $n = 1$ vortex model, this ratio is 2, whereas the Lamb–Oseen[38] and Vatistas $n = 2$ vortex models give values of 1.398 and 1.414, respectively (also see Appendix). From the present tests one can see that the Lamb–Oseen and the Vatistas $n = 2$ vortex models most adequately describe the measured vorticity distribution. Figure 15 shows the circulation as given by these models along with sample experimental results shown previously in Fig. 9.

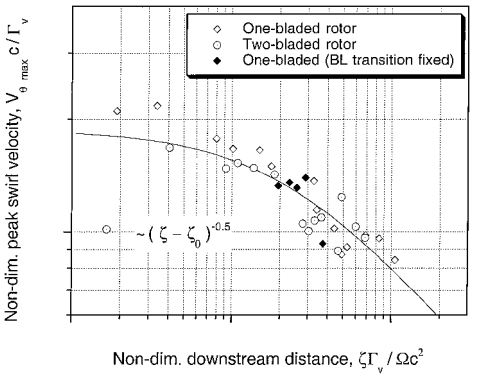

Fig. 16 Nondimensional peak swirl velocities in the tip vortices as a function of equivalent nondimensional downstream distance.

Correlation of Vortex Measurements

Figure 16 shows results in terms of the nondimensional peak swirl velocities in the vortex as a function of nondimensional downstream distance from the blade tip. Following an approach similar to that of Iversen,[39] the nondimensional velocity and distance (vortex age) are given by

$$\bar{V}_{\theta_{\max}} = \left(\frac{V_{\theta_{\max}}}{\Omega R}\right)\left(\frac{\Omega R c}{\Gamma_v}\right) = \frac{V_{\theta_{\max}} c}{\Gamma_v} \tag{2}$$

$$\bar{d} = (\zeta R/c)(\Gamma_v/\Omega R c) = \zeta\Gamma_v/\Omega c^2 \tag{3}$$

The correlation between the measurements performed with the different rotor configurations also supports the observed self-similarity of the tip-vortex structure. The decreasing trend in the peak swirl velocity, which is also observed in the fixed-wing case,[39] confirms that the tip vortices diffuse logarithmically with increasing vortex age. The present data show a trend that can be described by

$$\bar{V}_{\theta_{\max}}(\bar{d} + 2.197)^{\frac{1}{2}} = 2.782 \tag{4}$$

Iversen[39] reports a correlation region after a nondimensional distance of 50, where the measured vortex data showed the trend

$$\bar{V}_{\theta_{\max}}(\bar{d})^{\frac{1}{2}} = 5.8 \tag{5}$$

This decreasing trend in the peak swirl velocity can be interpreted as viscous diffusion. For constant vortex circulation strength the nondimensional peak velocity is inversely proportional to the core radius, and the distance $\bar{d}$ is proportional to the vortex age, i.e.,

$$\bar{V}_{\theta_{\max}} \propto 1/r_c, \qquad \bar{d} \propto \zeta$$

This implies that the core radius increases as the square root of the vortex age, i.e.,

$$r_c \propto \sqrt{\zeta} \tag{6}$$

The Lamb–Oseen result for viscous core growth is given by

$$r_c = \sqrt{4\alpha\nu(\zeta/\Omega)} \tag{7}$$

where $\alpha = 1.25643$ (see Appendix). This can be written in terms of nondimensional peak velocity and downstream distance as

$$\bar{V}_{\theta_{\max}}(\bar{d})^{\frac{1}{2}} = \frac{1 - e^{-\alpha}}{4\pi}\sqrt{\frac{1}{\alpha}\left(\frac{\Gamma_v}{\nu}\right)} = 0.05692\sqrt{\frac{1}{\alpha}\left(\frac{\Gamma_v}{\nu}\right)} \tag{8}$$

As shown by Squire,[40] Lamb's result can be modified to include an effective turbulent viscosity coefficient δ, which reflects a higher overall vorticity diffusion through turbulence generation compared to molecular diffusion alone, i.e., the latter equation can now be written as

$$\bar{V}_{\theta_{\max}}(\bar{d})^{\frac{1}{2}} = 0.05692\sqrt{(1/\alpha)(\Gamma_v/\delta\nu)} \tag{9}$$

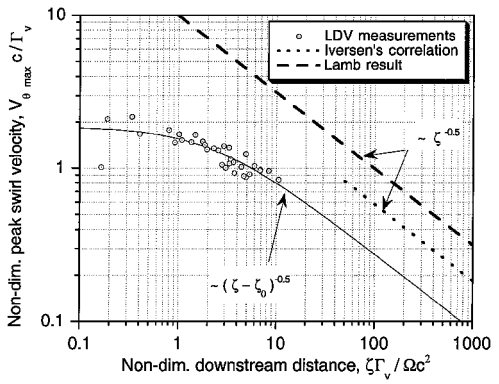

Fig. 17 Nondimensional peak swirl velocities in the tip vortex as a function of equivalent nondimensional downstream distance.

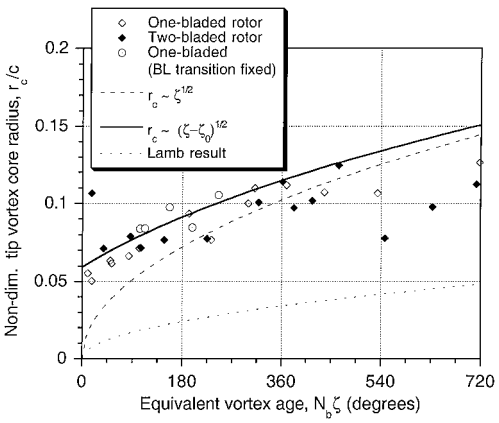

Fig. 18 Growth of the vortex core in terms of equivalent vortex age.

Comparing this with Iversen's results [Eq. (5)], it is apparent that Iversen's correlation is equivalent to including a turbulent viscosity coefficient that is proportional to the vortex Reynolds number, Γ_v/ν (also see Ref. 40). The peak velocity trend shown in Fig. 16 and given by Eq. (4) corresponds to the core growth trend

$$r_c = \sqrt{4\alpha\delta\nu[(\zeta - \zeta_0)/\Omega]} \tag{10}$$

where, for the present data, $\delta = 8.243$ and $\zeta_0 = 131.6$ deg. This curve is shown in Fig. 17 along with the Lamb result and Iversen's correlation. The ordinate shift ζ_0 results in an effective nonzero core radius at the tip-vortex origin ($\zeta = 0$ deg) and, therefore, a finite velocity at $\bar{d} = 0$. However, in the other two cases the swirl velocity is singular at the origin of the tip vortex and unrealistically high at small distances (vortex ages). At large downstream distances (vortex ages) all three curves show the same qualitative trend, i.e., the velocity is inversely related to $\sqrt{t}$, or equivalently, the core radius increases proportionally with $\sqrt{t}$.

Figure 18 shows the core growth trend derived from the preceding correlation trend, along with the Lamb-type trend with a constant turbulent viscosity. Again, the differences between the two curves are obvious at early equivalent vortex ages. At later ages the two curves have a qualitatively similar behavior. At large ages they will be almost coincident, i.e.,

$$r_c \propto \sqrt{\zeta/\Omega} \qquad \text{for} \qquad \zeta \gg \zeta_0 \tag{11}$$

Figure 19 shows the present measurements replotted along with recent rotor-tip-vortex measurements from Refs. 20 and 21. These results have been derived from the published measurements and have been reprocessed in terms of nondimensional velocity and downstream distance, as given by Eqs. (2) and (3), respectively. All three sets of measurements show a good correlation, and all of the results seem to follow the general logarithmic diffusion trend suggested earlier. The measurements at early vortex ages from Ref. 21 again bring out the $\sqrt{(t - t_0)}$ core growth trend suggested here, in contrast to the classical $\sqrt{t}$ core growth curve given by the Lamb

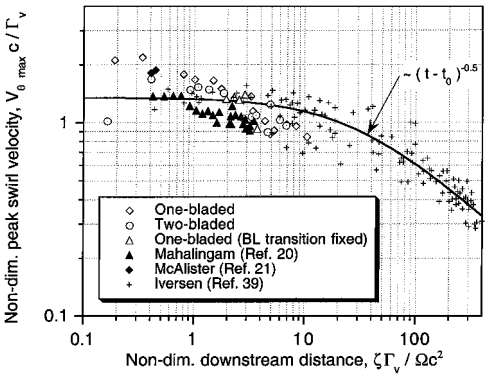

Fig. 19 General correlation of rotor-tip-vortex measurements in terms of nondimensional peak swirl velocities and equivalent nondimensional downstream distance.

model. The fixed-wing tip-vortex measurements reported in Ref. 39 are also shown for comparison. These fixed-wing measurements tend to have somewhat larger downstream distances as compared to the rotor measurements and, therefore, appear to show a $\sqrt{t}$-type growth curve. However, as seen from Fig. 19, a $\sqrt{(t - t_0)}$-type growth curve describes the fixed-wing data very well at both small and large distances.

Conclusions

Measurements of the tip vortices generated by subscale helicopter rotors operating in hover were performed using three-component LDV. Rotor-generated tip vortices are generally nonaxisymmetric in structure, at least at young vortex ages. In spite of this, the tip vortices were found to exhibit a self-similar swirl velocity structure. The strength of the tip vortices was found to be nominally constant for all measured ages, suggesting that energy dissipation is a slow process. However, the measurements showed that the tip vortices exhibited a notable viscous diffusion with increasing vortex age; the core swirl velocity was found to decrease logarithmically, and the core size was found to increase logarithmically. A general correlation curve was suggested to describe this behavior. This trend appears consistent with other documented measurements made of helicopter-rotor and fixed-wing tip vortices and lends confidence in the ability to describe their behavior by means of generalized semi-empirical models.

Appendix: Velocity Models

The Lamb–Oseen model of the swirl velocity in the vortex can be written as

$$V_\theta(\bar{r}) = \frac{\Gamma_v}{2\pi r_c}\left[\frac{1 - \exp(-\alpha\bar{r}^2)}{\bar{r}}\right] \tag{A1}$$

where $\alpha = 1.25643$ and $\bar{r}$ is the nondimensional radius based on the estimated core radius r_c at that vortex age.

A series of general desingularized velocity profiles is given in Ref. 37, where the swirl velocity in a two-dimensional cross-sectional plane of the vortex is expressed as

$$V_\theta(\bar{r}) = \frac{\Gamma_v}{2\pi r_c}\frac{r}{(1 + \bar{r}^{2n})^{\frac{1}{n}}} \tag{A2}$$

where n is an integer variable. The velocity profiles for three special vortex models with a particular value of n in the preceding equation can be written as follows.

1) $n \to \infty$, Rankine vortex:

$$V_\theta(\bar{r}) = \begin{cases} (\Gamma_v/2\pi r_c)\bar{r}, & 0 \le r \le r_c \\ (\Gamma_v/2\pi r_c)(1/\bar{r}), & r \ge r_c \end{cases} \tag{A3}$$

2) $n = 1$, Kauffman/Scully vortex:

$$V_\theta(\bar{r}) = \frac{\Gamma_v}{2\pi r_c}\frac{\bar{r}}{(1 + \bar{r}^2)} \tag{A4}$$

3) $n = 2$:

$$V_\theta(r) = \frac{\Gamma_v}{2\pi r_c} \frac{\bar{r}}{\sqrt{1+\bar{r}^4}} \tag{A5}$$

All of these velocity models satisfy the boundary conditions

$$V_\theta(\bar{r}) = \begin{cases} 0, & \bar{r} = 0 \\ V_{\theta_{\max}}, & \bar{r} = 1 \end{cases}$$

$$V_\theta(\bar{r}) \to 0 \qquad \text{as} \qquad \bar{r} \to \infty$$

The circulation at large $\bar{r}$ does not approach zero but asymptotes to a constant value Γ_v. However, the maximum swirl velocity at $\bar{r} = 1$ has different values for the different models. This results in a different net vortex circulation to core circulation ratio.

1) Lamb–Oseen vortex:

$$\Gamma_v / \Gamma_c = [1 - \exp(-\alpha)]^{-1} = 1.398 \tag{A6}$$

2) $n \to \infty$, Rankine vortex:

$$\Gamma_v / \Gamma_c = 1 \tag{A7}$$

3) $n = 1$, Kauffman/Scully vortex:

$$\Gamma_v / \Gamma_c = 2^{\frac{1}{n}} = 2 \tag{A8}$$

4) $n = 2$:

$$\Gamma_v / \Gamma_c = 2^{\frac{1}{n}} = 1.414 \tag{A9}$$

Acknowledgments

This work was supported by the National Rotorcraft Technology Center under Grant NCC 2944. The authors would like to thank Wayne Johnson for his suggestions regarding the core growth models.

References

[1]Leishman, J. G., and Bagai, A., "Challenges in Understanding the Vortex Dynamics of Helicopter Rotor Wakes," *AIAA Journal*, Vol. 36, No. 7, 1998, pp. 1130–1140.

[2]Schmitz, F. H, "Rotor Noise," *Aeroacoutics of Flight Vehicles: Theory and Practice*, Vol. 1, NASA Reference Publication, Aug. 1991, Chap. 2, p. 1258.

[3]Sheridan, P., and Smith, R., "Interactional Aerodynamics—A New Challenge to Helicopter Technology," *Proceedings of the 35th Annual American Helicopter Society Forum*, May 1979.

[4]Torok, M. S., and Ream, D. T., "Investigation of Empennage Airloads Induced by a Helicopter Main Rotor Wake," *Proceedings of the 49th Annual American Helicopter Society Forum*, May 1993.

[5]Scully, M. P., "A Method of Computing Helicopter Vortex Wake Distortion," Massachusetts Inst. of Technology, Rept. ASRL TR 138-1, Cambridge, MA, June 1967.

[6]Bliss, D. B., Dadone, L., and Wachspress, D. A., "Rotor Wake Modelling for High Speed Applications," *Proceedings of the 43rd Annual American Helicopter Society Forum*, May 1987.

[7]Johnson, W. R., "Wake Model for Helicopter Rotors in High Speed Flight," NASA CR-1177507, USAVSCOM TR-88-A-008, Nov. 1988.

[8]Clark, D. R., and Leiper, A. C., "The Free Wake Analysis—A Method for Prediction of Helicopter Rotor Hovering Performance," *Journal of the American Helicopter Society*, Vol. 15, No. 1, 1970, pp. 3–11.

[9]Berry, J. D., "Prediction of Time-Dependent Fuselage Pressures in the Wake of a Helicopter Rotor," *Proceedings of the 2nd International Conference on Basic Rotocraft Research*, Univ. of Maryland, College Park, MD, Feb. 1988.

[10]Egolf, T. A., "Rotor Wake Modelling for High Speed Applications," *Proceedings of the 44th Annual American Helicopter Society Forum*, May 1988.

[11]Bagai, A., and Leishman, J. G., "Adaptive Grid Sequencing and Interpolation Schemes for Accelerated Rotor Free-Wake Analyses," *AIAA Journal*, Vol. 36, No. 9, 1998, pp. 1593–1602.

[12]Dosanjh, D. S., Gasparek, E. P., and Eskinazi, S., "Decay of a Viscous Trailing Vortex," *Aeronautical Quarterly*, Vol. 3, No. 3, 1962, pp. 167–188.

[13]McAllister, K. W., and Takahashi, R. K., "NACA 0015 Wing Pressure and Trailing Vortex Measurements," NASA TP 3151, Nov. 1991.

[14]Sullivan, J. P., "An Experimental Investigation of Vortex Rings and Helicopter Rotor Wakes Using a Laser Doppler Velocimeter," Massachusetts Inst. of Technology Aerophysics Lab., TR 183, MIT DSR 80038, Cambridge, MA, June 1973.

[15]Landgrebe, A. J., and Johnson, B. V., "Measurements of a Model Helicopter Rotor Flow Field with a Laser Doppler Velocimeter," *Journal of the American Helicopter Society*, Vol. 19, No. 3, 1974, pp. 39–43.

[16]Han, Y. O., Leishman, J. G., and Coyne, A. J., "On the Turbulent Structure of a Tip Vortex Generated by a Rotor," *AIAA Journal*, Vol. 35, No. 3, 1997, pp. 869–879.

[17]Coyne, A. J., Bhagwat, M. J., and Leishman, J. G., "Investigation into the Rollup and Diffusion of Rotor Tip Vortices Using Laser Doppler Velocimetry," *Proceedings of the 53rd Annual American Helicopter Society Forum*, May 1997.

[18]Seelhorst, U., Beesten, B., and Butefisch, K. A., "Flowfield Investigation of a Rotating Helicopter Rotor Blade by Three-Component Laser Doppler Velocimetry," *Proceedings of the 75th AGARD Fluid Dynamic Panel Symposium*, Oct. 1994.

[19]Thomson, T. L., Komerath, N. M., and Gray, R. B., "Visualization and Measurement of the Tip Vortex Core of a Rotor Blade in Hover," *Journal of Aircraft*, Vol. 25, No. 12, 1988, pp. 1113–1121.

[20]Mahalingam, R., and Komerath, N. M., "Measurements of the Near Wake of a Rotor in Forward Flight," AIAA Paper 98-0692, Jan. 1998.

[21]McAlister, K. W., Sculer, C. A., Branum, L., and Wu, J. C., "3-D Wake Measurements near a Hovering Rotor for Determining Profile and Induced Drag," NASA TP 3577, Aug. 1995.

[22]McAlister, K. W., "Measurements in the Near Wake of a Hovering Rotor," AIAA Paper 96-1958, June 1996.

[23]Leishman, J. G., Baker, A., and Coyne, A. J., "Measurements of Rotor Tip Vortices Using Three-Component Laser Doppler Velocimetry," *Journal of the American Helicopter Society*, Vol. 41, No. 4, 1996, pp. 342–353.

[24]Leishman, J. G., "On Seed Particle Dynamics in Tip Vortex Flows," *Journal of Aircraft*, Vol. 33, No. 4, 1996, pp. 823–825.

[25]Devenport, W. J., Rife, M. C., Liapis, S. I., and Follin, G. J., "The Structure and Development of a Wing-Tip Vortex," *Journal of Fluid Mechanics*, Vol. 312, 1996, pp. 67–106.

[26]Leishman, J. G., "On the Aperiodicity of Helicopter Rotor Wakes," *Experiments in Fluids*, Vol. 25, 1998, pp. 352–361.

[27]Mabey, D. G., "A Review of Scale Effects in Unsteady Aerodynamics," *Progress in Aerospace Sciences*, Vol. 28, No. 4, 1991, pp. 272–321.

[28]Pope, A., *Low-Speed Wind Tunnel Testing*, Wiley, New York, 1984, Chap. 7, pp. 445–457.

[29]Nakamura, Y., and Tomonari, Y., "The Effects of Surface Roughness on the Flow Past Circular Cylinders at High Reynolds Numbers," *Journal of Computational Physics*, Vol. 123, Oct. 1982, pp. 363–373.

[30]Braslow, A. L., and Knox, E. C., "Simplified Method for Determination of Critical Height of Distributed Roughness Particles for Boundary-Layer Transition at Mach Numbers from 0 to 5," NACA TN 4363, Sept. 1958.

[31]Braslow, A. L., Hicks, R. M., and Harris, Jr., R. V., "Use of Grit-Type Boundary-Layer-Transition Trips," NASA TN D-3579, 1966.

[32]Chandrasekhara, M. S., Wilder, M. C., and Carr, L. W., "Boundary-Layer-Tripping Studies of Compressible Dynamics Stall Flow," *AIAA Journal*, Vol. 34, No. 1, 1996, pp. 96–103.

[33]Orloff, K. L., "Trailing Vortex Wind Tunnel Diagnostics with a Laser Velocimeter," *Journal of Aircraft*, Vol. 11, No. 8, 1974, pp. 477–482.

[34]McCormick, B. W., Tangler, J. L., and Sherrieb, H. E., "Structure of Trailing Vortices," *Journal of Aircraft*, Vol. 5, No. 3, 1968, pp. 260–267.

[35]Corsiglia, V. R., Schwind, R. G., and Chigier, N. A., "Rapid Scanning, Three Dimensional Hot Wire Anemometer Surveys of Wing-Tip Vortices," *Journal of Aircraft*, Vol. 10, No. 12, 1973, pp. 752–757.

[36]Scully, M. P., and Sullivan, J. P., "Helicopter Rotor Wake Geometry and Airloads and Development of Laser Doppler Velocimeter for Use in Helicopter Rotor Wakes," Massachusetts Inst. of Technology Aerophysics Lab., TR 183, MIT DSR No. 73032, Cambridge, MA, Aug. 1972.

[37]Vatistas, G. H., Kozel, V., and Mih, W. C., "A Simpler Model for Concentrated Vortices," *Experiments in Fluids*, Vol. 11, 1991, pp. 73–76.

[38]Lamb, H., *Hydrodynamics*, 6th ed., Cambridge Univ. Press, 1932, pp. 592, 593.

[39]Iversen, J. D., "Correlation of Turbulent Trailing Vortex Vortex Decay Data," *Journal of Aircraft*, Vol. 13, No. 5, 1996, pp. 338–342.

[40]Squire, H. B., "The Growth of a Vortex in Turbulent Flow," *Aeronautical Quarterly*, Vol. 16, Aug. 1965, pp. 592–593.

A. Plotkin
Associate Editor